Appl. Phys. B (2015) 119:445–452
DOI 10.1007/s00340-015-6024-1

Applied Physics B
Lasers and Optics

CrossMark

Laser ablation and deposition of titanium dioxide with ultrashort pulses at 527 nm

D. K. Pallotti · X. Ni · R. Fittipaldi · X. Wang · S. Lettieri · A. Vecchione · S. Amoruso

Received: 8 October 2014 / Accepted: 22 January 2015 / Published online: 4 February 2015
© Springer-Verlag Berlin Heidelberg 2015

Abstract We report an experimental analysis on laser ablation and deposition of TiO_2 with ≈300-fs, 527-nm ultrashort laser pulses. We particularly address the following: (1) the dependence of the deposition rate on the laser fluence, in high-vacuum conditions; (2) the effect of an oxygen background gas pressure on the expansion of the ablated species and on the deposition rate. Two different regimes are observed for the dependence of the deposition rate in high vacuum: The first one governed by two-photon absorption occurring close to the ablation threshold is, then, followed by the second, thermal dependence at larger fluences. The propagation of the atomic and nanoparticulate plumes produced in ultrashort laser ablation are influenced in a quite different way by the background gas pressure, which eventually reflects on the variation of the deposition rate with pressure. Moreover, it is observed that the ablated material is predominantly composed of nanoparticles (≈70 %), similar to what was reported before in the case of elemental metallic targets. Finally, plume deposition results in the formation of nanoparticle-assembled films with a variation of the characteristics morphology with the background gas pressure.

D. K. Pallotti · X. Ni · S. Amoruso (✉)
Dipartimento di Fisica, Università degli Studi di Napoli Federico II, Complesso Universitario di Monte S. Angelo, Via Cintia, 80126 Naples, Italy
e-mail: amoruso@na.infn.it

D. K. Pallotti · X. Ni · X. Wang · S. Lettieri · S. Amoruso
CNR-SPIN, UOS Napoli Complesso Universitario di Monte S. Angelo, Via Cintia, 80126 Naples, Italy

X. Ni
School of Electronic Engineering, Tianjin University of Technology and Education, Tianjin 300222, China

R. Fittipaldi · A. Vecchione
CNR-SPIN, UOS Salerno, Via Giovanni Paolo II 132, 84084 Fisciano, SA, Italy

1 Introduction

The physical and chemical properties that emerge when the size of the material reduces down to the nanometer scale has triggered enormous efforts, aiming to the development of techniques for nanoparticles (NPs) preparation as well as to the analysis of nanostructures and nanomaterials characteristics. As the size of the building blocks decreases to the nanoscale, the specific surface area and surface-to-volume ratio of materials raise dramatically. The superior superficial area brought about by NPs is favorable to many applications where the reaction/interaction with other media is essential, for example, in environmental sensing, photocatalysis and energy materials. In this context, a huge effort has been devoted to semiconductor NPs and among others to titanium dioxide (TiO_2) [1]. TiO_2 is a low-cost semiconductor extensively employed as a highly advanced and functional material [1, 2], taking advantage of the number of its properties for a variety of applications in photocatalysis, photovoltaics, sensor technology, decomposition of organic pollutants, antifogging and self-cleaning agents to living environment and so forth [1–7]. Another reason why TiO_2 is promising in many applications originates from its chemical robustness and negligible hazard to people health. These advantages allow it to be used in wider situation and environment with respect to other materials.

Many approaches have been devised for the fabrication of TiO_2 NPs and nanostructures, such as sol–gel methods, and chemical and physical vapor deposition [1]. Among physical vapor deposition techniques, pulsed laser

deposition (PLD) with nanosecond pulse duration has been largely exploited in the preparation of TiO_2 nanostructures, showing the important influence of deposition conditions on the characteristics of the deposited material [8–11]. In particular, the properties of the deposits can be significantly influenced by the presence of a background gas. Recently, Di Fonzo et al. [12] have shown a rather fine control over the morphology of TiO_2 microstructures by appropriate tuning of the experimental parameters, namely the background gas pressure.

More recently, ultrashort laser ablation with intense, femtosecond (fs) pulses has been demonstrated as a versatile route to generate NPs of a number of materials [13–15]. Hence, this capability of ultrashort PLD has been applied to a wide range of materials including metals, semiconductors and oxides [16–22]. Previous studies on ultrashort PLD of TiO_2, carried out in high vacuum or at low oxygen background pressure ($\approx 10^{-2}$ mbar), have shown that nearly stoichiometric TiO_2 NPs with average diameters of ≈20–50 nm are produced [23, 24]. The NP-assembled films deposited in such experimental conditions show a granular morphology with the constituting NPs mutually agglomerated in a cauliflower-like structure. Here, we further explore the features of ultrashort laser ablation and deposition of TiO_2, by analyzing: (1) the variation of the deposition rate with laser fluence (in high vacuum); (2) the effect of the oxygen background gas pressure on deposition rate, and hence on NP-assembled film morphology.

2 Experimental methods

Ultrashort laser ablation of a commercial TiO_2 rutile target (SurfaceNet) is induced by pulses of ≈300 fs at 527 nm produced by a Nd/glass laser system (Light Conversion Twinkle) through compressed second-harmonic generation of the fundamental output laser pulse (1,054 nm, ≈0.9 ps). The laser beam is focused at $\approx 45^{\circ}$ onto the target surface with a 25-cm-focal-length lens. The incident laser pulse energy, E, is varied by using neutral density filters. The average fluence F is obtained as E/S, where $S = (4.4 \pm 0.4) \times 10^{-4}$ cm^2 is the spot area estimated by measurement of the laser impact region as a function of the laser pulse energy [25]. The target is placed on a rotating holder to avoid localized cratering during ablation. Moreover, for film deposition with a large number of laser pulses, the laser beam is also rastered on the target surface.

The analysis of the deposition-rate dependencies as a function of the laser pulse fluence (in high vacuum) and of the oxygen background gas pressure (from 10^{-3} to 10^{3} Pa) is carried out by using a quartz crystal microbalance (QCM) with a 6-mm-diameter active area located at 4 cm from the target surface. Due to the QCM-limited sensitivity, for the deposition-rate measurements, a few thousand laser pulses (≈3,000–6,000) are typically used. ICCD time-gated imaging [26, 27] is used to correlate the ablation plume expansion dynamics with pressure dependence of the deposition rate. Finally, NP-assembled films are produced by collecting the ablated material on silicon (100) substrates placed at 4 cm from the target surface, at room temperature. The films morphology is, then, examined by a Zeiss ΣIGMA field emission scanning electron microscope (FESEM).

3 Results and discussion

In the following, we first discuss the variation in the deposition rate with the laser pulse fluence, in high vacuum (Sect. 3.1). Then, we address the effects of the background gas pressure on deposition rate and film morphology (Sect. 3.2).

3.1 Deposition rate vs laser pulse fluence

Laser ablation of solid targets exhibits a threshold behavior: Ablation occurs only when the laser fluence is higher than a certain value, which depends on both wavelength and duration of the laser pulse, as well as on the properties of the irradiated material. Different methods have been devised for the determination of the ablation threshold, for example, visual inspection of the sample [28], fluence dependence of the crater depth and area [24, 29–33], plasma emission [33, 34] and so forth. Moreover, interesting information on the mechanisms involved in the ablation process can be also gained by following the dependence of some of these quantities on the laser pulse characteristics (e.g., intensity, wavelength, duration, etc.).

Here, we discuss the variation of the deposition rate, δ, as a function of the laser pulse fluence, F, in high-vacuum conditions. The results are reported in Fig. 1. It is observed that the deposition-rate dependence on the fluence shows the presence of two different regimes. If one assumes that the deposition rate δ is approximately proportional to the ablation rate, d, this is suggestive of two ablation regimes, similar to what is typically observed for ultrashort laser ablation of metallic targets [29, 30]. During ablation of TiO_2 with 150-fs, 780-nm laser pulses, Furusawa et al. [35] reported the observation of only one regime and discussed it within a multiphoton-absorption model. Nevertheless, two different regimes of the ablation rate vs fluence were previously observed for ultrashort laser ablation of materials characterized by a large bandgap (e.g., c-BN and AlN) with Ti/Sa laser pulses (110 fs, 790 nm) [36, 37]. Besides the low-fluence regime, which can be directly related to the photon absorption process, the presence of a second

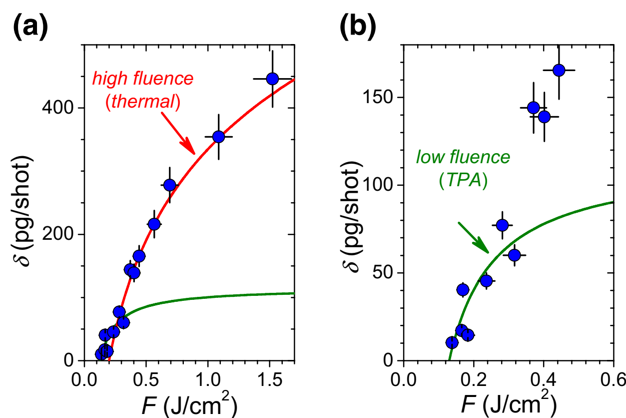

Fig. 1 **a** Dependence of the deposition rate, δ, as a function of the laser pulse fluence, F. The experimental results are reported as *circles*. The *green curve* is a fit to the TPA dependence [Eq. (7)], while the *red curve* is a fit to the logarithmic dependence [Eq. (2)] for the high-fluence regime; **b** zoom of the experimental data of (**a**) at low fluence

regime, at higher fluencies, was associated to the high thermal conductivity of these materials, similar to that of metals, which should favor a regime where the thermal diffusion length governs the ablation rate.

In the case of metals, the presence of the two different ablation regimes is typically associated to the two characteristic lengths of energy absorption into the target. At low laser fluence, the laser energy is absorbed within the optical skin depth (penetration depth) of the material, λ_{opt}; meanwhile, at high laser fluence, the energy is distributed over the electron thermal diffusion length, λ_{th} [29, 30]. Due to the linear absorption of the incident photons, an energy deposition profile of the Beer–Lambert form is assumed as:

$$E(z) = E_0 e^{-\frac{z}{\lambda}} \tag{1}$$

where z is the distance from the target surface, E_0 is the laser energy absorbed at the target surface ($z = 0$), and λ is the characteristic length of energy deposition, i.e., λ_{opt} at low fluence and λ_{th} at high fluence, respectively. Therefore, the depth d at which the energy is equal to the threshold energy for ablation, E_{th}, is

$$d = \lambda \ln\left(\frac{E_0}{E_{th}}\right) = \lambda \ln\left(\frac{F_0}{F_{th}}\right) \tag{2}$$

where F_0 and F_{th} are the average laser fluence of the incident beam and the threshold fluence for ablation, respectively.

For oxides with a bandgap larger than the incident photon energy, the threshold fluence has been shown to depend on both the pulse characteristics (wavelength and pulse duration) and material bandgap [38]. A linear scaling with the bandgap was observed and ascribed to the multiphoton-absorption coefficient dependence on the bandgap. The bandgap energy of TiO_2 is typically 3.0 eV, corresponding to two photons of the 527-nm laser light (2.35 eV). Following Furusawa [35], we can assume that two-photon absorption (TPA) process predominates in the case of TiO_2; thus, the variation of the laser intensity $I(z)$ near the target surface can be approximated as:

$$\frac{dI(z)}{dz} \approx -n\sigma_2 I^2(z) \tag{3}$$

which in terms of the average laser fluence F and pulse duration τ_p ($F = I\tau_p$) reads as:

$$\frac{dF(z)}{dz} \approx -\frac{n\sigma_2}{\tau_p} F^2(z) = b_2 F^2(z) \tag{4}$$

leading to

$$F(z) \approx \frac{F_0}{1 + b_2 F_0 z} \tag{5}$$

where F_0 is the fluence at $z = 0$. Ablation occurs when the fluence exceeds a threshold value $F_{th,TPA}$; therefore, the ablation depth, d_{TPA}, as a function of the fluence F in this case reads as:

$$d_{TPA} \approx \frac{1}{b_2}\left(\frac{1}{F_{th,TPA}} - \frac{1}{F_0}\right) \tag{6}$$

On the base of the previous discussion, one should expect for the low-fluence regime that

$$\delta = A\left(\frac{1}{F_{th,TPA}} - \frac{1}{F}\right) \tag{7}$$

a dependence which describes fairly well the experimental results (see Fig. 1b), with $F_{th,TPA} = (0.13 \pm 0.01)$ J/cm^2 and $A = (1.5 \pm 0.4) \times 10^{-11}$ g cm^2/J. This, indeed supports the hypothesis that the TPA mechanisms are dominant at low fluence. The measured fluence threshold is comparable to the damage threshold of TiO_2 ($\approx$0.12 J/cm^2) obtained by analysis of ablation crater area with pulses of $\approx$300 fs at 527 nm and $\approx$80 fs at 400 nm [23, 24].

As the laser fluence increases, TPA leads to promotion of a large number of electrons in the conduction band, which then spread the energy into the target over a larger depth with a characteristic electron thermal diffusion length, λ_{th}. Then, at higher fluence a thermal regime similar to that observed for metals ensues, that is, described by:

$$\delta \propto \ln\left(\frac{F}{F_{th}}\right) \tag{8}$$

as indicated by the good agreement with the experimental data in Fig. 1a (red curve), with $F_{th} = (0.20 \pm 0.01)$ J/cm^2. Hence, one can consider that for TiO_2 the laser energy is absorbed through multiphoton absorption in a skin layer, leading to a first regime at low fluence governed by multiphoton absorption. Then, at larger fluence, the high

thermal conductivity of the material triggers an effective transfer of the energy into the material, leading to the presence of a second, thermal regime with a logarithmic dependence similar to that observed in metallic targets.

3.2 Oxygen background pressure effects on deposition rate and film morphology

The confining effect of the background gas can have important effects on the expansion of ablation plume and, hence, on the number of ablated particles reaching the substrate.

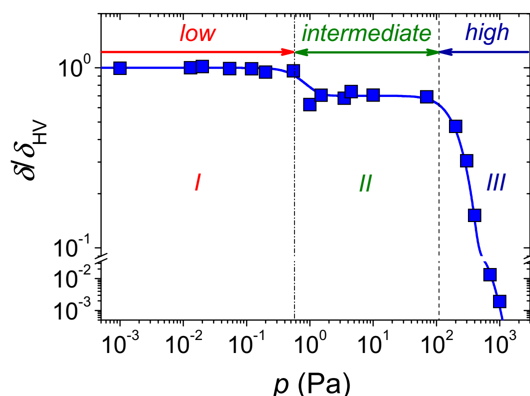

Fig. 2 Dependence of the deposition rate, δ, as a function of the oxygen background gas pressure, p. The deposition rate is normalized to the value registered in high vacuum, δ_{HV}. Three different deposition regimes are identified as indicated by the *arrows*. The *curve* is a guide to the eye

Both these parameters can influence the deposition dynamics and, thus, the properties of the deposited nanostructures.

The dependence of the deposition rate δ as a function of the background gas pressure p is obtained by measuring the overall amount of material deposited on a QCM located at the substrate position, for a laser fluence $F \approx 1.4$ J/cm^2 (see Fig. 2). The deposition rate is normalized to the value registered in high vacuum (HV), δ_{HV}. At low pressure, the deposition rate is constant to the high-vacuum value until the influence of the background gas on the propagation of the ablated species remains negligible. This happens up to a pressure $p \approx 0.5$ Pa, when the deposition rate starts decreasing and eventually approaches a second plateau regime for $p > 1$ Pa. In this intermediate regime, the deposition rate reduces to $\approx$70 % of that observed in HV conditions. Then, for $p > 110$ Pa a high-pressure regime ensues where the deposition rate drastically depends on the pressure. In fact, it reduces to $\approx$10 % of the HV value at $p \approx 400$ Pa, becoming $\approx$1 % for $p \approx 700$ Pa.

Figure 3 reports typical FESEM images of TiO_2 NP-assembled films elaborated in the three different regimes observed in the pressure dependence of the deposition rate (see Fig. 2). The number of laser shots, N, used for NP-assembled films deposition is rescaled according to the corresponding deposition rate. At low pressure, N is $\approx 4 \times 10^4$ (i.e., 20-min deposition at 33-Hz repetition rate). In the low-pressure regime (Figs. 3a, e), the film morphology is rather porous and composed of assembly of globular structures decorated with a number of smaller NPs with typical sizes of $\approx$10–20 nm. The transition to intermediate

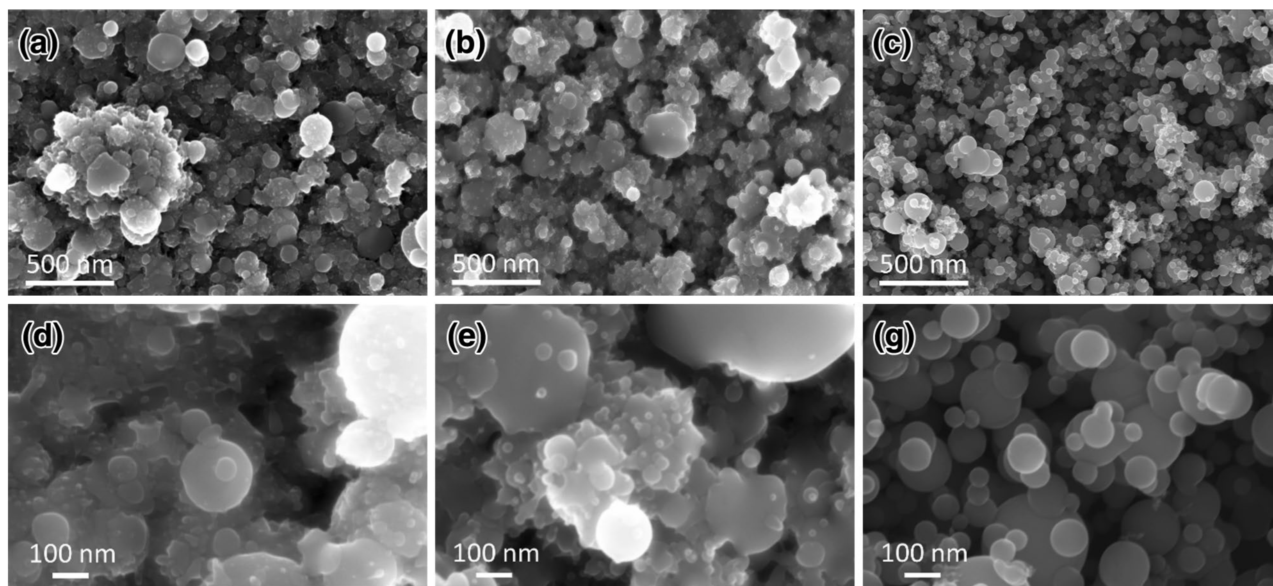

Fig. 3 Representative FESEM images of TiO_2 NP-assembled films elaborated in the low-pressure (**a** and **d**), intermediate-pressure (**b** and **e**) and high-pressure (**c** and **g**) regimes of the deposition-rate dependence. Lower panels show images acquired at higher magnification

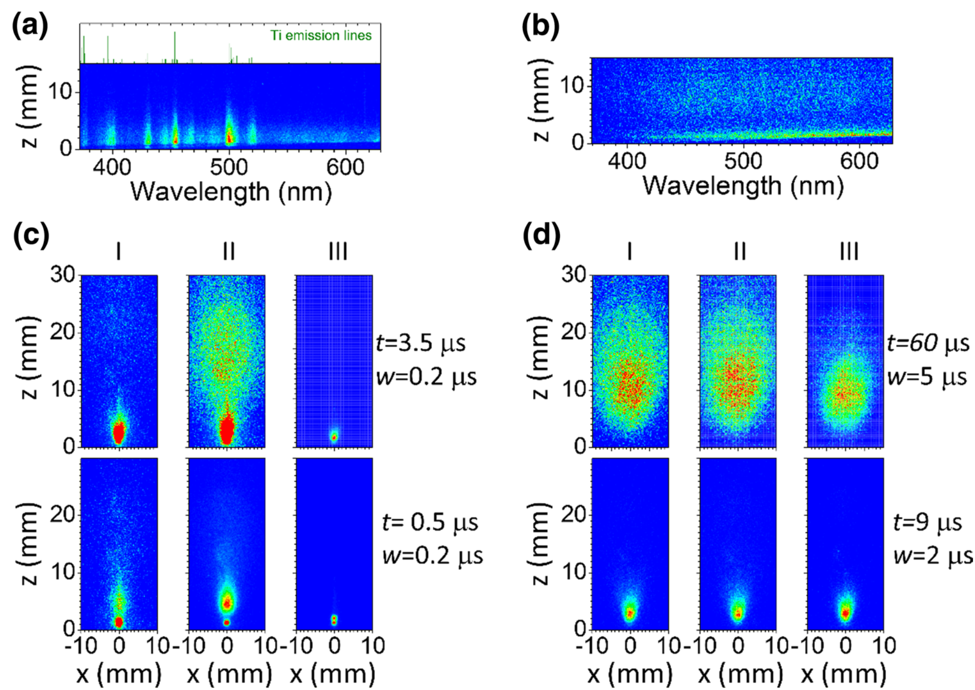

Fig. 4 Upper panels (**a**) and (**b**) report typical spectrally resolved 1D images of the atomic and NPs plumes emission, respectively. The upper inset of (**a**) reports Ti emission lines from Ref. [37]. Panel (**a**) shows intense Ti emission lines, while **b** illustrate the characteristic structureless, broadband emission of the NP plume. Lower panels show temporal sequences of the atomic (**c**) and NPs (**d**) plume emission for the three different regimes of the deposition rate vs background gas pressure, *p* (low pressure, I; intermediate pressure, II; high pressure, III). The time on the left side of the snapshots corresponds to the delay *t* after the laser pulse, and *w* is the gate width used for the acquisition. In (**c**), each image is normalized to the maximum intensity of the atomic plume; therefore, the NPs plume emission intensity is saturated

pressures does not affect significantly the film morphology (Figs. 3b, f), which continues to resemble an agglomerated, colloidal-like nanostructure with NPs embedded in a glue-like substance. In both cases, a number of rather shapeless and compact clusters are also present. Instead, the morphology of films deposited at high pressure is drastically different (Figs. 3c, g). The deposit is formed by many spherically shaped NPs with a typical size ranging from ≈20 to ≈200 nm. These NPs assemble into a packed-ball porous network, giving rise to a highly porous nanostructure of individual NPs.

ICCD time-gated imaging and spectroscopy allows a further assessment of the changes the background gas pressure induces on the propagation dynamics of the ablated species. As shown earlier [31], TiO_2 fs ablation plume comprises two main components: (a) a first population of atomic and molecular species, leaving the target surface with rather high expansion velocities (≈10^3–10^4 m/s); (b) a second, slower plume component constituted of NPs, expanding at smaller velocities (≈10^2 m/s). This is exemplified in the upper panels of Fig. 4, which report typical spectrally resolved 1D images of the ablated species emission registered in the range ≈370–630 nm at early and late delays. Figure 4a shows intense Ti emission lines as indicated by comparison with the upper inset, reporting Ti emission lines listed in Ref. [39]. Figure 4b illustrates the characteristic structureless, broadband emission of the NP plume. Figures 4c, d show two-dimensional (2D) images of the atomic and NP plumes, respectively, registered at two different delays, *t*, after the laser pulse in the three regimes of low (I), intermediate (II) and high (III) pressure. The time on the left side of the image corresponds to the delay *t* after the laser pulse, and *w* is the gate width used for the acquisition.

The three regimes of the deposition rate and film morphology can be correlated to the diverse influence of the background gas pressure on the atomic and NPs plumes propagation into the background gas [40–43].

We first discuss the atomic plume. At low pressure (regime I), the atomic plume is characterized by a rather forward-peaked expansion, reaching a distance of ≈1 cm from the target surface on a timescale of about 0.5 µs. At longer delays (e.g., $t = 3.5$ µs), only a very faint emission from the rear of the atomic plume, which has moved to larger distances while progressively decreasing in intensity, is discernible in Fig. 4c. At intermediate pressures (regime II), the interaction with the background gas leads to a progressive braking of the atomic plume which eventually

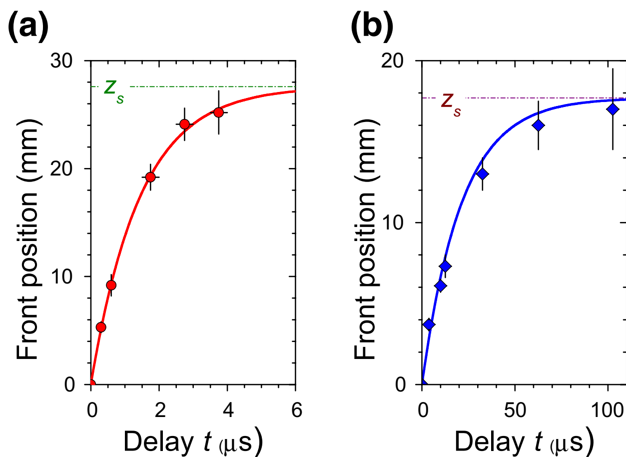

Fig. 5 Variation of the plume front position z as a function of delay t: **a** atomic plume at $p = 0.5$ Pa (transition between regimes I and II); **b** NP plume at $p = 10^3$ Pa (regime III). The curves are fits to the drag model $z(t) = z_s[1 - \exp(-\beta t)]$, while the dash–dot lines indicate the stopping distance. The *vertical error bars* account for uncertainties in the visual estimate of the luminous plume front position, while the *horizontal error bars* correspond to the acquisition gate width, w. For (**b**) the *horizontal error bars* are within the size of the experimental data points

becomes confined at late delays. This confining effect is clearly evidenced by the changes in the spatial distribution and shape of the atomic plume emission intensity. The gradual plume braking in this regime is illustrated in Fig. 5a by showing the variation of the atomic plume front position as a function of the delay t at $p = 0.5$ Pa, in the transitional region between low- and intermediate-pressure regimes. In a simplified approach, the ablation products can be regarded as an ensemble of particles experiencing a viscous force in the background gas proportional to velocity u (drag model) [44]. Then, the equation of the plume front velocity is $du/dt = -\beta u(t)$, β being a slowing coefficient. This gives $z(t) = z_s[1 - \exp(-\beta t)]$, where $z_s = u_0/\beta$ is the stopping distance and $u_0 = u(t = 0)$ is the initial velocity. The drag model describes pretty well the experimental data, with $z_s = (27.6 \pm 0.7)$ mm, $\beta = (0.69 \pm 0.04)$ x 10^{-6} s^{-1} and $u_0 = (1.9 \pm 0.2) \times 10^4$ m/s. This indicates that in regime II the atomic plume is halted over distances shorter than the target-to-substrate distance, and atomic species reach the substrate only through diffusion into background gas and in gradually less amount [45]. When the transition to regime II occurs, the atomic plume contribution to the deposited material becomes negligible, explaining the plateau in the deposition rate at intermediate pressure. The ≈30 % reduction in the deposition rate between the low and intermediate regimes points to a minor contribution of the atomic plume to the deposition rate. This, in turn, demonstrates that for TiO_2 the ejected material is primarily in form of NPs, similar to what was reported earlier for ultrashort laser ablation of metallic targets [33, 46, 47]. At larger pressures, the atomic plume is stopped over a distance of few mm, as illustrated in the images of Fig. 4(c) at $t = 0.5$ μs.

On the contrary, the NPs plume expansion (see Fig. 4d) remains almost unaffected by the background gas pressure up to $p \approx 100$ Pa, due to the extraordinary mass ratio between the NPs and the ambient gas molecules. Then, for $p > 10^2$ Pa the confining effects of the background gas starts affecting also the NPs plume propagation, as evidenced in Fig. 4. Figure 5b reports the NPs plume front position as a function of the delay t at $p = 10^3$ Pa, in the high-pressure regime. Also in this case, the drag model provides a reliable description of the NPs plume front dynamics with $z_s = (17.7 \pm 0.9)$ mm, $\beta = (4.7 \pm 0.5) \times 10^{-8}$ s^{-1} and $u_0 = (8 \pm 1) \times 10^2$ m/s, thus indicating that it is halted over a distance of few centimeters. It is therefore likely that as the pressure level reaches few hundred Pa, the background gas starts effectively confining the NP plume and the probability that NPs reach the substrate through diffusion in the background gas progressively reduces. This, in turn leads to the drastic reduction in the deposition rate observed in the high-pressure regime at larger p.

The change in the propagation dynamics of the NP plume also explains the variation in the film morphology between low-/intermediate-pressure and high-pressure regimes. In regimes I and II, the NPs expand in the background gas at high velocity being eventually deposited along a line-of-sight trajectory and impacting the substrate at high kinetic energy. On the contrary, in regime III the NP plume is halted over distances shorter than the target-to-substrate distance and the NPs are eventually collected on the substrate after diffusion into the background atmosphere. This explains the noteworthy change of the film morphology, suggesting that appropriate tuning of the experimental parameters (e.g., background gas pressure or target-to-substrate distance) can allow additional control on the morphology of the nanostructures produced by fs PLD.

4 Summary

We studied ultrashort laser ablation and deposition of TiO_2 at a visible laser pulse wavelength (527 nm), which was seldom investigated. The interest for TiO_2 lies in the fact that it is a low-cost semiconductor extensively employed as a highly advanced and functional material.

Here, we have first addressed the dependence of the deposition rate on the laser pulse fluence, in high-vacuum conditions. Two different regimes are observed. The first one is governed by two-photon absorption and occurs close to the ablation threshold. Then, the second, thermal regime ensues at larger fluences.

Secondly, we have considered ultrashort laser ablation for the elaboration of TiO_2 NP-assembled films, illustrating the effect on deposition rate and film morphology of an oxygen background gas pressure, *p*. Three different regimes of deposition rate are identified which results in different NP-assembled film morphology, which passes from a structure with glue-like nanoparticulates, at low pressure, to a highly porous assembly of individual, spherical NPs, at larger pressure. The pressure variation of deposition rate and film morphology is rationalized by analysis of the expansion of the ablated species with time-gated imaging. This allows observing that atomic and NP plumes are influenced in a quite different way by the background gas pressure. At low and intermediate pressure ($p < 100$ Pa), the NPs expand in the background gas at high velocity being eventually deposited along a line-of-sight trajectory and impacting the substrate at high kinetic energy. On the contrary, at high pressure ($p > 100$ Pa), the NP plume is halted over distances shorter than the target-to-substrate distance and the NPs are eventually collected on the substrate after diffusion into the background atmosphere. This explains the noteworthy change of the film morphology, suggesting that appropriate tuning of the experimental parameters (e.g., background gas pressure or target-to-substrate distance) can allow additional control on the morphology of the nanostructures produced by fs PLD. Finally, it is assessed that the ablated material is predominantly composed of nanoparticles (≈70 %), similar to what was reported earlier in the case of elemental metallic targets.

Acknowledgments The work has been partially supported by the Italian MIUR through the FIRB Project RBAP115AYN "Oxides at the nanoscale: multifunctionality and applications" and the PRIN 2010 Project "OXIDE".

References

1. X. Chen, S.S. Mao, Chem. Rev. **107**, 2891 (2007)
2. O. Carp, C.L. Huisman, A. Reller, Prog. Solid State Chem. **32**, 33 (2004)
3. R. Wang, K. Hashimoto, A. Fujishima, M. Chikuni, E. Kojima, A. Kitamura, M. Shimohigoshi, T. Watanabe, Nature **388**, 431 (1997)
4. M. Grätzel, Nature **414**, 338 (2001)
5. A. Hagfeldt, M. Grätzel, Chem. Rev. **95**, 49 (1995)
6. A.L. Linsebigler, G. Lu, J.T. Yates Jr, Chem. Rev. **95**, 735 (1995)
7. A. Mills, R.H. Davies, D. Worsley, Chem. Soc. Rev. **22**, 417 (1993)
8. M. Walczak, E.L. Papadopoulou, M. Sanz, A. Manousaki, J.F. Marco, M. Castillejo, Appl. Surf. Sci. **255**, 5267 (2009)
9. E. Gÿorgy, A. Pérez del Pino, G. Sauthier, A. Figueras, F. Alsina, J. Pascual, J. Phys. D Appl. Phys. **40**, 5246 (2007)
10. D.G. Syarif, A. Miyashita, T. Yamaki, T. Sumita, Y. Choi, H. Itoh, Appl. Surf. Sci. **193**, 287 (2002)
11. M. Sanz, M. Walczak, M. Oujja, A. Cuesta, M. Castillejo, Thin Solid Films **517**, 6546 (2009)
12. F. Di Fonzo, C.S. Casari, V. Russo, M.F. Brunella, A. Li Bassi, C.E. Bottani, Nanotechnology **20**, 015604 (2009)
13. S. Amoruso, G. Ausanio, R. Bruzzese, M. Vitiello, X. Wang, Phys. Rev. B **71**, 033406 (2005)
14. S. Eliezer, N. Eliaz, E. Grossman, D. Fisher, I. Gouzman, Z. Henis, S. Pecker, Y. Horovitz, M. Fraenkel, S. Maman, Y. Lereah, Phys. Rev. B **69**, 144119 (2004)
15. S. Amoruso, R. Bruzzese, N. Spinelli, R. Velotta, M. Vitiello, X. Wang, G. Ausanio, V. Iannotti, L. Lanotte, Appl. Phys. Lett. **84**, 4502 (2004)
16. M. Sanz, M. Lòpez-Arias, J.F. Marco, R. de Nalda, S. Amoruso, G. Ausanio, S. Lettieri, R. Bruzzese, X. Wang, M. Castillejo, J. Phys. Chem. C **115**, 3203 (2011)
17. M. Sanz, R. de Nalda, J.F. Marco, J.G. Izquierdo, L. Bañares, M. Castillejo, J. Phys. Chem. C **114**, 4864 (2010)
18. J. Perrière, C. Boulmer-Leborgne, R. Benzerga, S. Tricot, J. Phys. D Appl. Phys. **40**, 7069 (2007)
19. Y. Zhang, R.E. Russo, S.S. Mao, Appl. Phys. Lett. **87**, 133115 (2005)
20. J. Perrière, E. Millon, W. Seiler, C. Boulmer-Leborgne, V. Craciun, O. Albert, J.C. Loulergue, J. Etchepare, J. Appl. Phys. **91**, 690 (2002)
21. E. Millon, J. Perrière, R.M. Défourneau, D. Défourneau, O. Albert, J. Etchepare, Appl. Phys. A Mater. Sci. Process. **77**, 73 (2003)
22. S. Amoruso, G. Ausanio, R. Bruzzese, L. Lanotte, P. Scardi, M. Vitiello, X. Wang, J. Phys. Condens. Matter **18**, L49 (2006)
23. M. Sanz, M. Castillejo, S. Amoruso, G. Ausanio, R. Bruzzese, X. Wang, Appl. Phys. A **101**, 639 (2010)
24. M. Sanz, M. Walczak, R. de Nalda, M. Oujja, J.F. Marco, J. Rodríguez, J.G. Izquierdo, L. Bañares, M. Castillejo, Appl. Surf. Sci. **255**, 5206 (2009)
25. M. Liu, Opt. Lett. **7**, 196 (1982)
26. J. Siegel, G. Epurescu, A. Perea, F.J. Gordillo-Vázquez, J. Gonzalo, C.N. Afonso, Opt. Lett. **29**, 2228 (2004)
27. S. Amoruso, C. Aruta, R. Bruzzese, D. Maccariello, L. Maritato, F. Miletto Granozio, P. Orgiani, U. Scotti di Uccio, X. Wang, J. Appl. Phys. **108**, 043302 (2010)
28. B.C. Stuart, M.D. Feit, S. Hermann, A.M. Rubenchik, B.W. Shore, M.D. Perry, Phys. Rev. B **53**, 1749 (1996)
29. S. Nolte, C. Momma, H. Jacobs, A. Tunnermann, B.N. Chichkov, B. Wellegehausen, H. Welling, J. Opt. Soc. Am. B **14**, 2716 (1997)
30. K. Furusawa, K. Takahashi, H. Kumagai, K. Midorikawa, M. Obara, Appl. Phys. A **69**, S359 (1999)
31. M. Sanz, M. Castillejo, S. Amoruso, G. Ausanio, R. Bruzzese, X. Wang, Appl. Phys. A **101**, 639 (2010)
32. J. Bonse, S. Baudach, J. Krüger, W. Kautek, M. Lenzner, Appl. Phys. A **74**, 19 (2002)
33. S. Amoruso, R. Bruzzese, X. Wang, N.N. Nedialkov, P.A. Atanasov, J. Phys. D Appl. Phys. **40**, 331 (2007)
34. P.P. Pronko, S.K. Dutta, J. Squier, J.V. Rudd, D. Du, G. Mourou, Opt. Commun. **114**, 106 (1995)
35. K. Furusawa, K. Takahashi, S.-H. Cho, H. Kumagai, K. Midorikawa, M. Obara, J. Appl. Phys. **87**, 1604 (2000)
36. Y. Hirayama, H. Yabe, M. Obara, J. Appl. Phys. **89**, 2943 (2001)
37. Y. Hirayama, M. Obara, J. Appl. Phys. **90**, 6447 (2001)
38. M. Mero, J. Liu, W. Rudolph, D. Ristau, K. Starke, Phys. Rev. B **71**, 115109 (2005)
39. D.R. Lide (ed.), *CRC Handbook of Chemistry and Physics*, 85th edn. (CRC Press, Boca Raton, 2005)
40. S. Amoruso, J. Schou, J.G. Lunney, Europhys. Lett. **76**, 436 (2006)
41. S. Amoruso, C. Aruta, R. Bruzzese, X. Wang, U. Scotti di Uccio, Appl. Phys. Lett. **98**, 101501 (2011)

42. D.B. Geohegan, A.A. Puretzky, G. Duscher, S.J. Pennycook, Appl. Phys. Lett. **72**, 2987 (1998)
43. S. Amoruso, J. Schou, J.G. Lunney, Appl. Phys. A **92**, 907 (2008)
44. D.B. Geohegan, Appl. Phys. Lett. **60**, 2732 (1992)
45. S. Amoruso, B. Toftmann, J. Schou, Phys. Rev. E **69**, 056403 (2004)
46. M.E. Povarnitsyn, T.E. Itina, M. Sentis, K.V. Khishchenko, P.R. Levashov, Phys. Rev. B **75**, 235414 (2007)
47. S. Amoruso, R. Bruzzese, X. Wang, J. Xia, Appl. Phys. Lett. **92**, 041503 (2008)